

# SyMRI of the Brain

## Rapid Quantification of Relaxation Rates and Proton Density, With Synthetic MRI, Automatic Brain Segmentation, and Myelin Measurement

Akifumi Hagiwara, MD,\*† Marcel Warntjes, PhD,‡§ Masaaki Hori, MD, PhD,\*  
Christina Andica, MD,\* Misaki Nakazawa, BS,\*|| Kanako Kunishima Kumamaru, MD, PhD,\*  
Osamu Abe, MD, PhD,† and Shigeki Aoki, MD, PhD\*

**Abstract:** Conventional magnetic resonance images are usually evaluated using the image signal contrast between tissues and not based on their absolute signal intensities. Quantification of tissue parameters, such as relaxation rates and proton density, would provide an absolute scale; however, these methods have mainly been performed in a research setting. The development of rapid quantification, with scan times in the order of 6 minutes for full head coverage, has provided the prerequisites for clinical use. The aim of this review article was to introduce a specific quantification method and synthesis of contrast-weighted images based on the acquired absolute values, and to present automatic segmentation of brain tissues and measurement of myelin based on the quantitative values, along with application of these techniques to various brain diseases. The entire technique is referred to as “SyMRI” in this review. SyMRI has shown promising results in previous studies when used for multiple sclerosis, brain metastases, Sturge-Weber syndrome, idiopathic normal pressure hydrocephalus, meningitis, and postmortem imaging.

**Key Words:** SyMRI, synthetic MRI, quantitative MRI, QRAPMASTER, brain, relaxation rates, proton density, automatic brain segmentation, myelin measurement, multiple sclerosis

(*Invest Radiol* 2017;52: 647–657)

This review article provides an overview of the QRAPMASTER (quantification of relaxation times and proton density by multiecho acquisition of a saturation-recovery using turbo spin-echo readout) method for tissue relaxometry,<sup>1</sup> including synthesis of contrast-weighted images, automatic segmentation of brain tissues, and measurement of myelin based on the quantitative values acquired. The

entire technique is referred to as “SyMRI” in this article. Clinical applications of SyMRI in previous studies are also reviewed. SyMRI now has regulatory approval in several countries and can be integrated into a PACS system and used on GE, Philips, and Siemens platforms.

The signal intensity of conventional magnetic resonance (MR) images depends on many acquisition parameters and MR scanner variations. Thus, absolute signal intensity has no direct meaning, and evaluation of magnetic resonance imaging (MRI) scans mainly involves comparison with surrounding tissues in the same slice. Absolute quantification of longitudinal relaxation time (T1), transverse relaxation time (T2), or their inverse relaxation rates (R1 and R2), and proton density (PD) provides an absolute scale and hence enables a more objective evaluation of disease. Absolute quantification of tissue properties has been previously reported for characterization of lesions<sup>2,3</sup> and monitoring of treatment.<sup>4</sup>

The fundamentals of absolute measurement of R1<sup>5,6</sup> and R2<sup>7</sup> relaxation rates that are currently used were described in the mid-1900s. Methods for rapid measurement of R1<sup>8–14</sup> and R2 or R2\*<sup>13–21</sup> relaxation rates and PD<sup>13,15</sup> have recently been established and performed in a research setting. Methods for simultaneous measurement of R1, R2, and PD have also been proposed.<sup>22,23</sup> In many cases, the excessive scan time required for quantitative MRI or high background noise has hampered its clinical use.<sup>13</sup> Development of a new pulse sequence, known as QRAPMASTER,<sup>1</sup> enables simultaneous quantification of R1, R2, and PD in a scan time of around 6 minutes for full head coverage with good accuracy and reproducibility,<sup>24</sup> enabling clinical use.

In addition to the practical issues of application of a rapid sequence, clinicians have only limited experience in reading absolute R1, R2, and PD maps and may want to confirm their findings by conventional contrast-weighted images, which increases the total examination time. This problem can be solved by synthesis of contrast-weighted images based on the same quantitative values. Synthesis of MRI scans based on absolute quantitative values also enables formation of consistent images that are free from imperfections in the scanner and variations in the pulse sequence.<sup>25,26</sup> Synthetic images can also be tailored to each patient for various diseases.<sup>27</sup> Synthetic MRI is also very promising in pediatrics because contrast images can be optimized after the actual scanning is performed, which is advantageous for visualizing the developing brain.<sup>28</sup>

Using quantitative maps as input for automatic segmentation, algorithms remove issues concerning sensitivity of the coil, inhomogeneity in radiofrequency, and differences in contrast throughout the volume imaged. Automatic segmentation has been reported to be precise and robust.<sup>29–31</sup> Furthermore, automatic segmentation of brain volume, gray matter (GM), white matter (WM), and myelin is expected to be of increasing value in terms of the clinical workflow.

### Magnetic Resonance Quantification

A schematic description of the QRAPMASTER sequence is shown in Figure 1. This includes 2 phases that are repeated over complete quantification of tissue parameters. In the first phase, a

Received for publication December 26, 2016; and accepted for publication, after revision, February 2, 2017.

From the \*Department of Radiology, Juntendo University School of Medicine; †Department of Radiology, Graduate School of Medicine, The University of Tokyo, Tokyo, Japan; ‡SyntheticMR AB; §Center for Medical Imaging Science and Visualization, Linköping, Sweden; and ||Department of Radiological Sciences, Graduate School of Human Health Sciences, Tokyo Metropolitan University, Tokyo, Japan.

Conflicts of interest and sources of funding: Marcel Warntjes is currently employed part-time at SyntheticMR and has a stock in SyntheticMR. This work was supported by the Japan Society for the Promotion of Science KAKENHI (grant number 16K19852) and Grant-in-Aid for Scientific Research on Innovative Areas—resource and technical support platforms for promoting research “Advanced Bioimaging Support” (grant number JP16H06280), and it was also funded by the Impulsing Paradigm Change Through Disruptive Technologies (ImPACT) Program of the Council for Science, Technology, and Innovation (Cabinet Office, Government of Japan).

Correspondence to: Akifumi Hagiwara, MD, Department of Radiology, Juntendo University School of Medicine, 1-2-1, Hongo, Bunkyo-ku, Tokyo, Japan, 113–8421. E-mail: a-hagiwara@juntendo.ac.jp.

Copyright © 2017 The Author(s). Published by Wolters Kluwer Health, Inc. This is an open-access article distributed under the terms of the Creative Commons Attribution-Non Commercial-No Derivatives License 4.0 (CCBY-NC-ND), where it is permissible to download and share the work provided it is properly cited. The work cannot be changed in any way or used commercially without permission from the journal.

ISSN: 0020-9996/17/5210-0647

DOI: 10.1097/RLI.0000000000000365

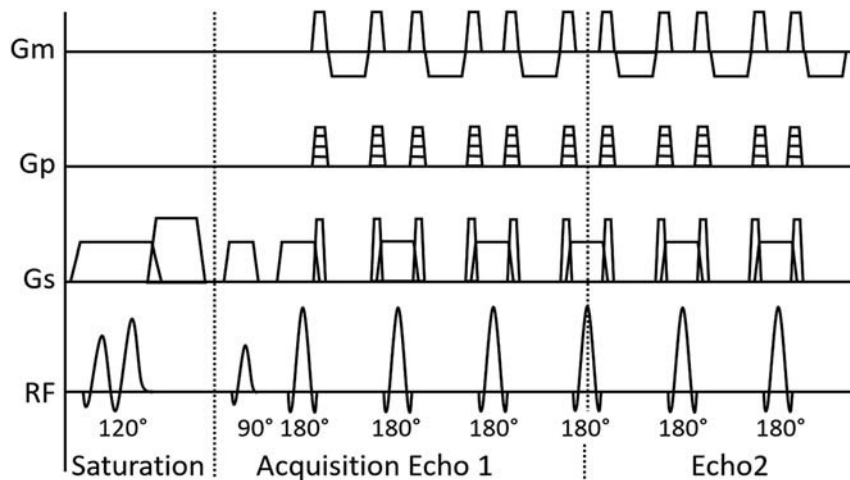


**FIGURE 1.** Schematic illustration of a single basic block of the QRAPMASTER quantification pulse sequence. Gradients of measurement (Gm), phase-encoding (Gp), and slice-selection (Gs), and the radiofrequency pulse amplitude over time are shown. One block consists of 2 phases. In the first phase (saturation), the 120-degree saturation pulse  $\theta$  is performed on a slice  $m$ , followed by subsequent spoiling. In the second phase, an acquisition is performed on slice  $n$ , providing an effective saturation delay time for each specific slice. Typically, 4 delay times are acquired and turbo spin-echo acquisition consists of 2 echoes. The acquisition uses the 90-degree excitation pulse  $\alpha$  and multiple 180-degree refocusing pulses. The acquired  $k$ -space lines can be combined to fewer echoes than the number of refocusing pulses. The spin-echo acquisition can also be accelerated through an echo-planar imaging technique (GraSE, not depicted).

slice-selective saturation pulse with flip angle  $\theta$  acts on a slice  $m$ , followed by spoiling of the signal (“saturation”). In the second phase, a slice-selective turbo spin-echo acquisition of another slice  $n$  (“acquisition”) is performed, which consists of multiple echoes. By introducing a shift between slice  $m$  and  $n$ , a delay is introduced between the saturation and acquisition of each slice. In this way, a matrix of images is acquired with different effects of R1 and R2 relaxation. The acquisition can be accelerated using an echo-planar imaging technique that acquires several  $k$ -space lines per spin-echo (gradient spin-echo [GRaSE]). However, acceleration by reconstructing fewer echo images than refocusing pulses is more commonly used. Typically, 2 echoes are reconstructed while using 10 or 12 refocusing pulses.

Because this method applies a saturation pulse rather than an inversion pulse, the starting position of the R1 relaxation curve will be a function of the B1 field and hence, it is possible to measure the local B1 field at the same time. The estimated B1 field can be used for correction of the effects of local deviations in flip angle. Based on R1, R2, and B1, it is possible to extract the unsaturated magnetization ( $M_0$ ), which is proportional to the PD. Note that QRAPMASTER independently measures R1 and R2 relaxation rates, which prevents propagation of error between these 2 parameters. Furthermore, because quantification of R1 and R2 relaxation rates and PD is performed simultaneously when using this method, the resulting maps are coregistered (Fig. 2). This is an advantage over earlier methods of quantification that required separate scans for these measurements.<sup>14</sup> The sequence is inherently black-blood, but inflow effects may be so high that flow artifacts may occur, mainly in the first slices in the neck. A regional saturation pulse can be added to the QRAPMASTER acquisition to constantly saturate the inflowing blood to avoid blood flow artifacts.

A spin system simulation of the whole sequence was performed to correct the nonideal behavior of the slice-selective radiofrequency pulses on the quantitative values, as well as to relate the observed saturation flip angle  $\theta_{\text{eff}}$  to the effective excitation flip angle  $\alpha_{\text{eff}}$ .

Each quantitative MRI with a QRAPMASTER pulse is performed with a number of combinations of echo times and delay times. For example, 2 echo times and 4 delay times are used to generate 8 complex images for measuring R1 and R2 relaxation rates in possible physiologic and pathologic ranges with the minimal acquisition time. A least

square fit is performed on the signal intensity (I) of these images by minimizing the following equation:

$$I = A \cdot PD \cdot \exp(-R_2 TE) \frac{1 - \{1 - \cos(B_1 \theta)\} \exp(-R_1 TI) - \cos(B_1 \theta) \exp(-R_1 TR)}{1 - \cos(B_1 \alpha) \cos(B_1 \theta) \exp(-R_1 TR)}$$

The above equation can be used to retrieve longitudinal R1 relaxation rate, transverse R2 relaxation rate, PD, and the amplitude of the local radiofrequency B1 field.<sup>1</sup> The applied excitation flip angle  $\alpha$  and the saturation flip angle  $\theta$  are obtained from the scanner.  $A$  is an overall intensity scaling factor that takes into account several elements, including sensitivity of the coil, amplification of the radiofrequency chain, and voxel volume.

An interleaved slice order is often used to avoid slice cross-talk but would lead to varying error in the R1 curves per slice in quantification of MRI. Therefore, the slice order of the quantification scan is chosen linearly so that the error becomes similar for each slice.

Using the QRAPMASTER method, monoexponential decay is assumed for the R1 and R2 relaxation times and only a limited number of relaxation data points are used, whereas R1 and R2 relaxation might be multiexponential under the various microscopic environments encountered in vivo.<sup>15,32</sup> Therefore, the measured relaxation rates reflect the dominant component of the relaxation behavior, which may lead to partial volume errors. The multiexponential effect is particularly strong at the interface between brain tissue and cerebrospinal fluid (CSF). Furthermore, relaxation of the very short-lived myelin water will be mainly invisible using the method. However, a validation study that used a phantom and healthy volunteers has demonstrated that this method is sufficiently accurate and reproducible for use in clinical practice, even with different head coils.<sup>24</sup>

Quantitative MRI enables direct comparison between brains in an objective manner because it gives absolute numbers for relaxation behavior and water content. Quantitative maps of healthy subjects can be spatially normalized into a standard stereotactic space for producing maps of normal brain tissue as references, in which differences in the size and shape of each individual brain can be ignored.<sup>33,34</sup> These maps can be compared with those of another individual or group of people. Another advantage of this approach is that analysis of atlas-based

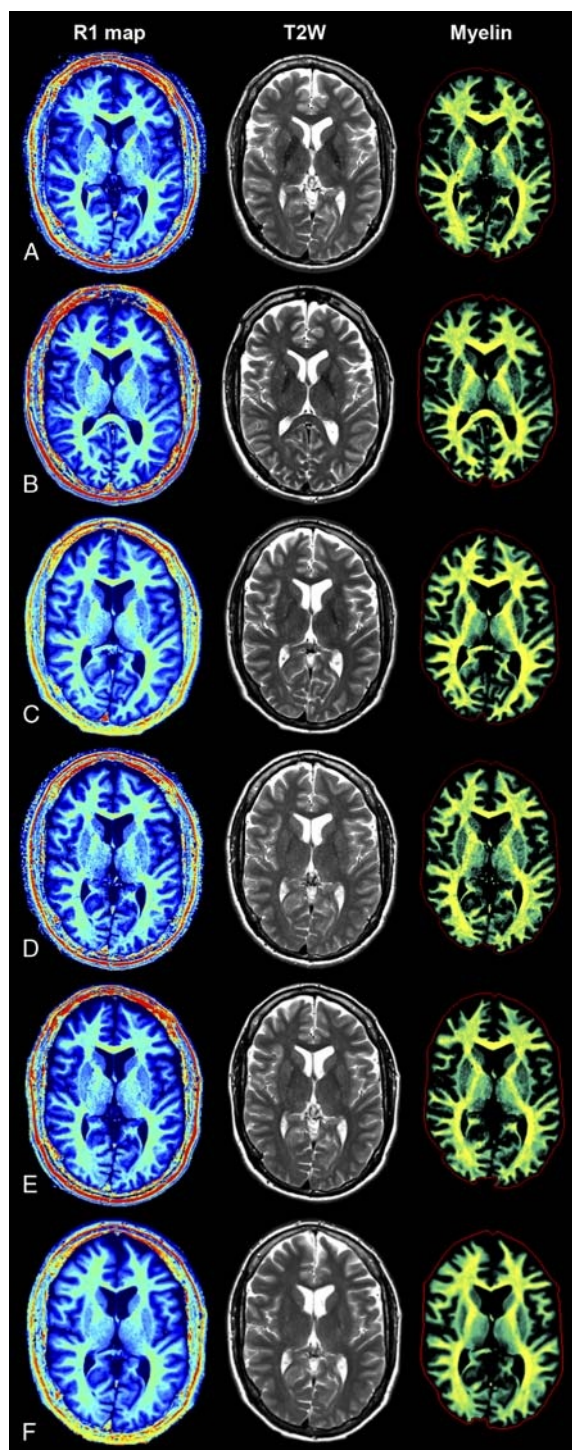


**FIGURE 2.** Quantification using SyMRI. The QRAPMASTER acquisition was applied to retrieve the R1 map (left column), R2 map, and PD map. Based on these maps, conventional (eg, T2-weighted) images can be synthesized (center column). Furthermore, the R1, R2, and PD maps provide an absolute scale and hence a robust input to brain segmentation. An example of one of these segmentations (of myelin) is shown in the right column. The SyMRI method provides maps that are independent of the magnetic resonance scanner and hence provide the same result on all major platforms. For this example, the subject was scanned at 3.0 T on a GE 750 (A), Siemens Skyra (B), Philips Ingenia (C), and at 1.5 T on a GE 450 W (D), Siemens Aera (E), and Philips Ingenia (F).

regions of interest (ROIs) can be performed unambiguously instead of subjectively defining these regions. This also enables automatic detection of brain pathology by artificial intelligence.

Before development of the QRAPMASTER pulse sequence, tissue relaxometry had been used in studies of patients with diseases such as epilepsy,<sup>35</sup> multiple sclerosis (MS),<sup>36–39</sup> Parkinson disease,<sup>40</sup> autism,<sup>41</sup> and schizophrenia,<sup>42</sup> as well as in patients with trauma<sup>43</sup> and brain tumors.<sup>44,45</sup> Use of SyMRI for evaluation of diseases of the brain will be discussed later in this review.

## Image Synthesis

Radiologists have limited experience in handling absolute R1 and R2 values and PD. Therefore, most radiologists would still want to make a diagnosis in clinical practice based on conventionally weighted contrast images rather than quantitative maps. Synthetic MRI can address this issue. Quantification of R1 and R2 values and PD can be used to calculate the signal intensity of a pixel by virtually setting any combination of echo time and repetition time (assume flip angle  $\alpha = 90$  degrees) to create T1-weighted, T2-weighted, or PD-weighted images using the following equation<sup>1</sup>:

$$S = PD\{1 - \exp(-R_1 TR)\} \exp(-R_2 TE)$$

Inversion recovery images, such as fluid-attenuated inversion recovery (FLAIR) and short-tau inversion recovery, can also be synthesized by adding an inversion recovery time (TI) based on the equation:

$$S = PD\{1 - 2 \exp(-R_1 TI) + \exp(-R_1 TR)\} \exp(-R_2 TE)$$

Furthermore, a double inversion recovery (DIR)<sup>27,46,47</sup> can be synthesized using 2 inversion delay times (TI<sub>1</sub> and TI<sub>2</sub>) according to the following equation:

$$S = PD\{1 - 2 \exp(-R_1 TI_1) + 2 \exp(-R_1 TI_2) - \exp(-R_1 TR)\} \exp(-R_2 TE)$$

Synthetic MRI has the potential to diminish the overall MR scan time, especially when multiple contrast-weighted images are needed, which is often the case in the clinical setting. A shorter scan time can be an advantage of synthetic MRI, especially in pediatric or noncooperative patients.<sup>48</sup> A long postprocessing time<sup>49</sup> has limited the clinical use of synthetic MRI, but postprocessing now takes less than 1 minute using SyMRI software (SyntheticMR, Linköping, Sweden).<sup>50</sup> At 1.5 T, although synthetic T1-weighted and T2-weighted images have a contrast-to-noise ratio (CNR) similar to that of conventional images, synthetic FLAIR images have a lower CNR than conventional FLAIR images, because of the higher noise level of synthetic MRI at 1.5 T.<sup>50</sup> However, DIR images that suppress signals from WM and CSF, when tailored to each patient, have higher CNR than conventional DIR at 3.0 T.<sup>27</sup> Several radiologists independently made a diagnosis based on synthetic and conventional MRI on different occasions for 22 adult<sup>50</sup> and 32 pediatric<sup>28</sup> patients. As a result, diagnosis based on synthetic and conventional MRI showed good agreement.

Synthetic T1-weighted and FLAIR images have more parallel imaging and motion artifacts than conventional images.<sup>50</sup> Furthermore, the surface of the brain is hyperintense on synthetic FLAIR images.<sup>27</sup> This artifact is presumably caused by a partial volume effect of brain tissue with CSF. The surface of the brain is even brighter on synthetic DIR images that suppress signals of WM and CSF. However, this may not be a large drawback if the existence of this artifact is known in advance of image reading. In addition, synthetic FLAIR images are sometimes degraded by basilar artery and CSF pulsation artifacts.<sup>30</sup> Other artifacts affecting synthetic images include chemical-shift displacement, Gibbs ringing phenomenon along the superior sagittal sinus, and a sinusoidal intensity difference in the CSF in PD-weighted and T2-weighted images in the anteroposterior direction.<sup>30</sup>

## Brain Segmentation

Neurodegenerative diseases, such as Alzheimer disease,<sup>51</sup> vascular dementia,<sup>52</sup> and MS,<sup>53</sup> are associated with focal and global brain atrophy. Therefore, estimation of brain volume as a whole and on a tissue basis would contribute to early diagnosis and follow-up of these diseases, as well as comparison with reference groups. A plethora of methods for brain segmentation has been proposed, most of which work on conventional MRI scans with one<sup>54</sup> or more contrast weightings.<sup>55,56</sup> Each voxel can be assigned to 1 specific tissue type<sup>54,55</sup> or a mixture of tissue types.<sup>56</sup> Because partial volume is common in the brain, allowing more than 1 tissue in 1 voxel removes the dependence on spatial resolution, which decreases the imaging time required for high resolution. Allowing only one tissue type in each voxel may elicit partial volume errors. However, 2 or more contrast weightings are usually required to make a multidimensional feature space for calculating tissue fractions. Although conventional contrast-weighted images provide good anatomic detail, the signal intensity is not absolute and the segmentation is performed based on differences in contrast between different tissues, which require provisional filters and normalization of signal intensities.<sup>55,57</sup> However, quantitative MRI results in absolute values for all tissue properties, which are independent of imperfections intrinsic to the scanner or variations in the pulse sequence.<sup>1</sup>

Brain segmentation can be performed based on the quantitative values measured by the QRAPMASTER method (Fig. 3).<sup>58</sup> Fully automatic brain segmentation and volumetry is now implemented in SyMRI software, and the postprocessing time is less than 1 minute, which is much shorter than the widely used volumetric methods with conventional MRI, such as FreeSurfer, FMRIB Software Library (FSL), or statistical parametric mapping.<sup>30</sup> The SyMRI can be launched in the PACS system and integrated into the clinical workflow. Normal brain tissues show a relatively narrow range of R1 and R2 values and PD,<sup>59,60</sup> whereas pathological tissues show significantly deviated values.<sup>1,61</sup> The measured quantitative values of brain tissues can be used as coordinates in a 3-dimensional feature space, that is, the R1-R2-PD space. Previously reported quantitative values for WM, GM, and CSF

measured by SyMRI for healthy controls<sup>1</sup> were used to define each brain tissue, and a numerical Bloch simulation was performed to investigate R1, R2, and PD for tissue mixtures and their ratio.<sup>58</sup> Based on the simulation, a lookup grid was created for relating tissue partial volumes to the R1-R2-PD space. Simulation of added noise causes random variations in R1, R2, and PD, resulting in tissue clusters with a finite distribution.<sup>62</sup> Voxels within the 95% prediction ellipses of the reference clusters for each tissue type were categorized as 100% pure tissue. Simulated pure tissue and partial volume clusters are combined to show curved bands in the R1-R2-PD space. Between these bands, 95% of voxels containing WM, GM, and CSF acquired with a simulated signal-to-noise ratio of 20 are expected to fall. The curves between the mean values of the pure tissue clusters without added noise lie in the midline.

This method calculates tissue fractions in each voxel, whereby fractions alter in 0.1% increments from 0 to 100. Voxels that were not categorized as WM, GM, or CSF or mixtures hereof in the grid were termed non-WM/GM/CSF (NoN). The volume fraction of each tissue type multiplied by the volume in each voxel was summated to show the total volumes of WM, GM, CSF, or NoN. The brain parenchymal volume (BPV) was calculated as the sum of WM, GM, and NoN.

The border of the intracranial volume (ICV) is defined exactly at a PD of 50%, assuming that the border of the ICV corresponds to the interface between CSF (PD = 100%) and bone (PD = 0%).<sup>29</sup> The ICV is automatically cut at the base of the skull.<sup>63</sup> The ICV corresponds to the sum of BPV and CSF. The brain parenchymal fraction (BPF) is calculated as the ratio of BPV to ICV. Automatic quantification of ICV at 3.0 T performed by SyMRI software was in good agreement with the reference manual method.<sup>29</sup> The processing time was less than 1 minute and much shorter than that of FSL or FreeSurfer. The short processing time is an obvious advantage for use in clinical practice.

Within-subject coefficients of variation in tissue volumes measured by this method at 1.5 T for multiple in-plane resolutions and 3 acquisition geometries (axial, sagittal, and coronal) were small.<sup>58</sup> This method also showed excellent repeatability for 2 scans both at 1.5 T<sup>63</sup> and at 3.0 T.<sup>30</sup> The repeat measurement errors for BPV, ICV, BPF, and

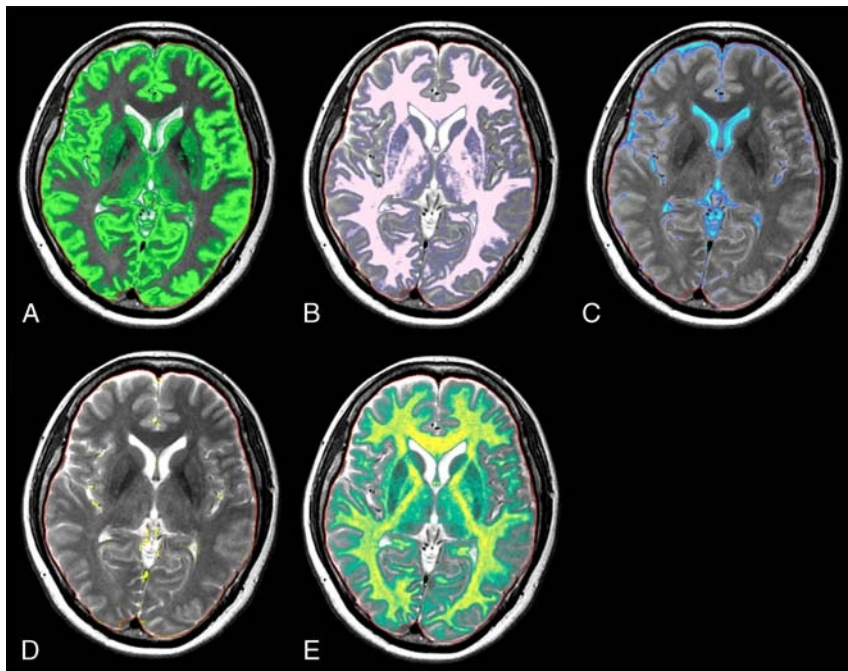


**FIGURE 3.** Segmentation results from a healthy volunteer for gray matter (A), white matter (B), cerebrospinal fluid (C), non-white matter/gray matter/cerebrospinal fluid (D), and myelin (E). Background synthetic T2-weighted images are imposed as references. The red lines indicate intracranial volume.

the GM fraction measured by SyMRI at 3.0 T were significantly lower than those measured by FreeSurfer, FSL, or SPM.<sup>30</sup>

It is not sufficient to measure the BPV when evaluating atrophy of the brain because the ICV varies widely from individual to individual and it is difficult to determine whether pathological atrophy beyond age-dependent physiologic atrophy has occurred. Normalizing BPV with the ICV largely removes size-dependence, making BPF a suitable measure for assessing brain atrophy. The reference range of BPF stratified by age was investigated by Vågberg et al,<sup>64</sup> who compared the results obtained by 3 automated segmentation methods, that is, SyMRI, voxel-based morphometry, and SPM, and by manual segmentation. The BPF decreased progressively with increasing age using all the volumetric methods; however, of the 3 automated techniques, SyMRI correlated the most with manual segmentation. The BPF value derived from SyMRI was not significantly different from that derived using the manual method and was the highest of all the 3 automated methods.

The R1 and R2 values measured depend on the magnetic field strength, with R1 lower and R2 higher on 3.0 T than on 1.5 T. This effect depends on tissue architecture and is not necessarily linear. Therefore, longitudinal studies and patient follow-up by MR volumetry can be affected by changes in the field strength of the system.<sup>65</sup> Therefore, to compensate for differences in field strength, separate lookup grids have to be implemented for brain segmentation. Brain segmentation results on SyMRI performed at 1.5 and 3.0 T were compared based on different lookup grids.<sup>66</sup> Although most of the brain segmentation was identical between the 2 sets of results and each result had high repeatability, marked regional differences were noted in deep brain structures, that is, the cerebellum and brain stem. Specifically, these structures had a propensity to be segmented as WM on 3.0 T. This is presumably because of deposition of iron, which affects R1 and R2 values.<sup>67</sup> Overall, WM was overestimated, and GM and CSF were underestimated on 3.0 T when compared with 1.5 T, with relatively little change in BPV. Although the present method is promising for application at both field strengths, these regional differences should be considered when interpreting the results obtained when using different field strengths. However, the present segmentation method could reduce the differences in volume measurements between 1.5 T and 3.0 T systems to a greater extent than that possible with FreeSurfer, SPM, and Bayesian-based methods for whole brain volumes.<sup>66</sup>

Warntjes et al<sup>63</sup> investigated the effects of gadolinium (Gd) contrast on volumetry by SyMRI in patients with MS. The calculated ICV and CSF values were significantly lower and NoN was significantly higher in post-Gd than in pre-Gd volumetry. However, these changes were much smaller than the differences between patients with MS and controls. Leakage of Gd into brain tissue strongly increases the R1 relaxation rate, but no enhancing lesions were detected in the patients with MS in this study. Therefore, there may have been some amount of Gd in the capillary network or lymphatic system (the so-called glymphatic system<sup>68</sup>) in the brain, which resulted in the change in tissue properties and thus led to the change in the automated tissue classification.

## Quantitative Magnetic Resonance Spectroscopy

The results of MR spectroscopy (MRS) are usually presented as the ratio of metabolite concentrations because MRS alone cannot calculate absolute metabolite concentrations. The linear combination model is a method that analyzes the in vivo MRS signal as a combination of the complete spectra of metabolites in vitro.<sup>69</sup> Although total creatine is usually used as the internal reference, it varies with age<sup>70</sup> and shows interindividual variation in patients with MS.<sup>71</sup> Therefore, absolute quantification of the metabolite concentration is desirable. By combining quantitative MRI and MRS using the linear combination model, absolute metabolite concentrations can be calculated by calibrating the MRS with the properties of internal water.<sup>70</sup> Thus, this method does

not need an external phantom with a known metabolite concentration as a reference as is required by other methods.<sup>72,73</sup> Furthermore, tissue segmentation by SyMRI can correct for the partial volume effects from CSF in an MRS volume of interest. Magnetic resonance spectroscopy quantification with SyMRI has been used for examining the effect of aging on each metabolite<sup>70</sup> and change in metabolites in patients with MS.<sup>74</sup>

## Myelin and Edema Model

The content of myelin and edema in the brain can be estimated from R1, R2, and PD quantified by SyMRI.<sup>75</sup> This model assumes 4 compartments in the brain, that is, the myelin partial volume ( $V_{MY}$ ), the cellular partial volume ( $V_{CL}$ ), the free water partial volume ( $V_{FW}$ ), and the excess parenchymal water partial volume ( $V_{EPW}$ ) (Fig. 4). Of these, only the  $V_{MY}$  and  $V_{FW}$  can be automatically calculated in the latest version of the SyMRI software (version 8.0), and  $V_{CL}$  and  $V_{EPW}$  are still for research use only. In the diseased brain, decreased  $V_{MY}$ , indicating decreased myelin, or increased  $V_{EPW}$ , indicating edema, is incorporated into this model. The model postulates that each compartment has its own R1, R2, and PD and contributes to the effective R1, R2, and PD of each specific acquisition voxel, whereas exchanging magnetization with other partial volume compartments.  $V_{MY}$  contains the myelin water and myelin sheaths.  $V_{CL}$  contains intracellular water, extracellular water, and nonmyelin macromolecules. The myelin water is trapped between the myelin sheaths and therefore has more rapid relaxation than intracellular or extracellular water. The more commonly calculated myelin water fraction corresponds to PD in the  $V_{MY}$  divided by the PD in  $V_{CL}$  and  $V_{EPW}$ . The proportionality of the myelin water fraction to the actual myelin volume has been validated in vitro and by histopathological examination.<sup>76,77</sup> Because of its macromolecular component,  $V_{CL}$  has a medium relaxation time that is slower than for  $V_{MY}$  but still faster than  $V_{FW}$ . Furthermore, as no distinction can be made between excess parenchymal water and the parenchymal water already present in the  $V_{CL}$ , the magnetization exchange rate between  $V_{EPW}$  and  $V_{CL}$  is infinitely high. The CSF is physically separated from the brain parenchyma, and hence, there is no net exchange of magnetization between  $V_{FW}$  and other partial volume compartments. Brain quantification maps from a group of healthy controls were spatially normalized and averaged, after which the data were used for Bloch simulation and optimization of the model parameters. Although estimation of myelination stage is reported to be comparable between conventional and synthetic MRI scans,<sup>48</sup> the myelin volume calculated by this proposed method might improve estimation of the myelination stage.

The total aqueous content of the brain can be calculated and mapped by combining the PD values for all the 4 partial volume compartments. The remaining volume of the brain represents the total nonaqueous content, which can be attributed to macromolecules.

When  $V_{MY}$  is combined with neurite orientation dispersion and density imaging,<sup>78</sup> the axon volume fraction and g-ratio, which is the ratio of the axon diameter to the external nerve fiber diameter, can also be calculated.<sup>79</sup> Further investigation is required to determine whether these measures can describe the disease process more specifically than R1, R2, and PD.

There are many methods that can evaluate the volume of myelin in a brain other than SyMRI. Some of these are based on magnetization transfer imaging,<sup>80</sup> measurement of multiexponential T2 relaxation time,<sup>81</sup> or the ratio of T1-weighted and T2-weighted images.<sup>82</sup> To date, no study has compared the measurement of myelin by SyMRI with other methods or histology, and validation studies are still awaited.

## Clinical Applications

### Multiple Sclerosis

Multiple sclerosis is a demyelinating disorder of the CNS that usually affects young people. Detection of new or progressing focal

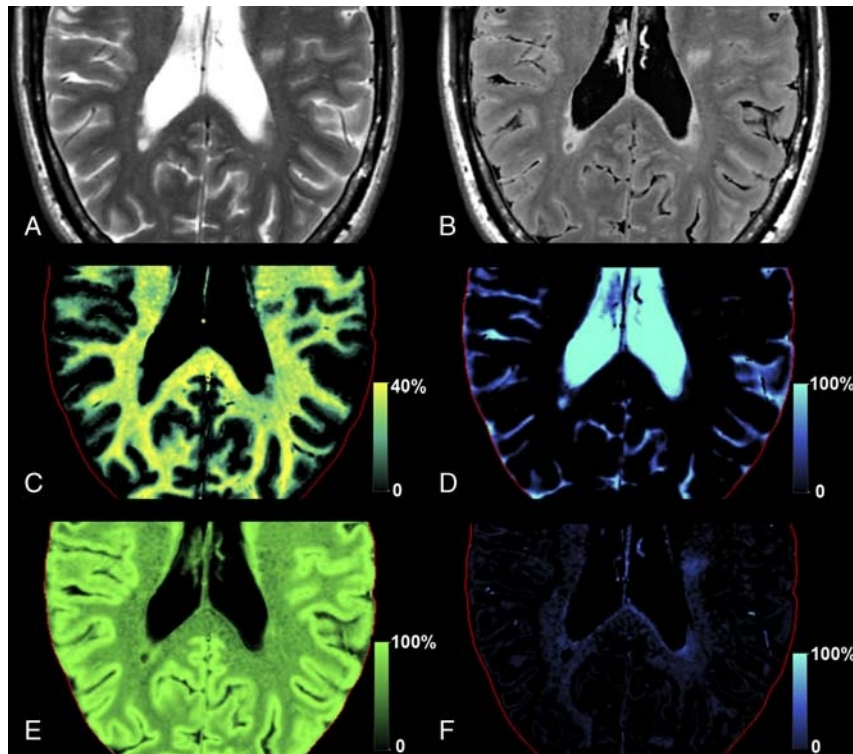


**FIGURE 4.** Myelin segmentation in a patient with multiple sclerosis. Synthetic T2-weighted (A) and fluid-attenuated inversion recovery (B) images of an axial slice of the brain of the patient based on measured R1, R2, and PD maps. Using the same data, the tissue is decomposed into the myelin partial volume  $V_{MY}$  (C), the free water partial volume  $V_{FW}$  (D), the cellular partial volume  $V_{CL}$  (E), and the excess parenchymal water partial volume  $V_{EPW}$  (F). The red line indicates the intracranial volume.

lesions is appropriate for diagnosing and evaluating the effects of treatment in MS.<sup>83</sup> Synthetic MRI enables detection of more MS plaques than conventional MRI with comparable or shorter acquisition times.<sup>27,30</sup> Double inversion recovery and phase-sensitive inversion recovery (PSIR) images are known to be useful for detecting MS plaques, especially those in cortical or mixed WM-GM areas.<sup>84</sup> Double inversion recovery suppresses signals from WM and the CSF, increasing the contrast between lesions and other brain tissues.<sup>85</sup> Phase-sensitive inversion recovery is a T1-weighted inversion recovery (T1IR) sequence with phase-sensitive reconstruction that increases the dynamic range of signal intensity and the tissue contrast by combining the positive and negative longitudinal magnetization.<sup>86</sup> However, DIR and PSIR images are not acquired routinely because of the limited amount of time available in the clinical setting. An advantage of synthetic MRI is that it can create DIR and PSIR in addition to other contrast-weighted images (Fig. 5).<sup>27</sup>

Patients with MS have been shown by SyMRI volumetry to have significantly lower BPF than healthy age-matched controls,<sup>31,87</sup> as previous studies using other methodologies had already shown.<sup>88,89</sup> Brain atrophy is a prognostic factor for future disability,<sup>90</sup> and the rate of loss of brain volume could be reduced by drug treatment.<sup>91</sup> Significant linear relationships between BPF and age, duration of disease, and Expanded Disability Status Scale scores were also observed.<sup>31</sup> Patients with relapsing-remitting MS had a higher BPF than those with secondary or primary progressive MS, indicating that patients with relapsing-remitting disease had less atrophy.<sup>31</sup> A previous study reported similar results.<sup>92</sup> As mentioned in another report,<sup>89</sup> a higher Expanded Disability Status Scale score and a longer disease duration correlated with a higher degree of atrophy.<sup>31</sup>

In patients with MS, lesions were mainly categorized as either NoN or a combination of NoN and CSF in the segmentation images

on SyMRI.<sup>31,58,63</sup> The rims of some lesions were attributed to NoN and the center parts attributed to CSF, especially the ones that were hypointense on T1-weighted images.<sup>63</sup>

For detecting active MS plaques, a Gd-based contrast agent is generally used to show the breakdown of the blood-brain barrier in these lesions. However, Gd contrast agents carry a potential risk of adverse events,<sup>93</sup> and deposition of Gd in the brain tissue has also been confirmed.<sup>94</sup> The tissue properties of MS plaques with and without enhancement after administration of Gd-based contrast agent were investigated by Blystad et al<sup>95</sup> with the aim of evaluating the possibility of detecting active lesions without a Gd contrast agent. Before administration of a Gd-based contrast agent, enhancing plaques had significantly higher R1 and R2 and lower PD than nonenhancing plaques. An area under the receiver operating characteristic curve of 0.832 for predicting enhancement was obtained by combining these quantitative values. Although this value is not satisfactory enough to warrant immediate introduction of this technique into clinical use, it can be an alternative way of detecting active lesions if a patient has a contraindication to Gd-based contrast agents.

Although MRI is a sensitive method for detecting MS plaques, the correlation between number of plaques and disease severity is but modest. This phenomenon is known as “clinico-radiological paradox,”<sup>96</sup> and quantitative MRI could be a solution. Quantitative MRI with the QRAPMASTER method has been used to evaluate patients with MS.<sup>2,3,74,87</sup> Quantitative MRS, which uses internal water for calibration when measuring absolute metabolite concentrations, has demonstrated increased glutamate and glutamine (Glx) in the normal-appearing WM of patients with MS.<sup>74</sup> After categorizing these patients into typical MS with multiple MS plaques (MRI<sub>pos</sub>) and atypical MS with few or no MS plaques (MRI<sub>neg</sub>), an increase in Glx was found in both groups. Furthermore, Glx was positively correlated with disease

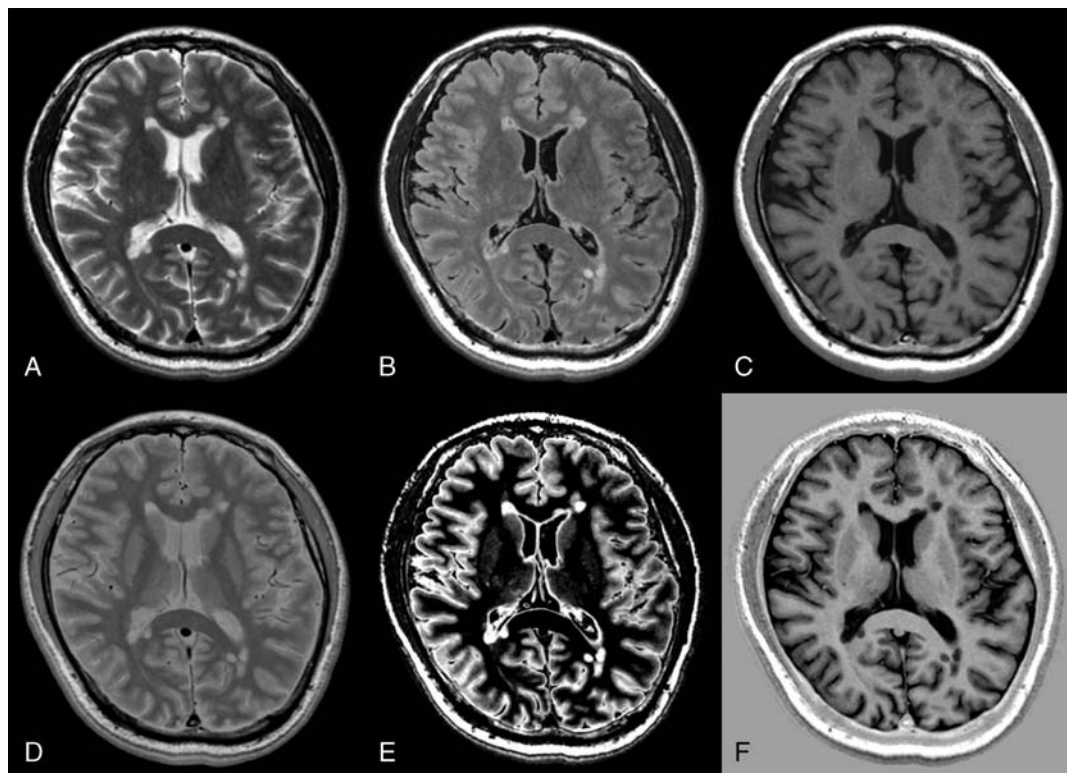


**FIGURE 5.** Representative slices of synthetic T2-weighted (A), fluid-attenuated inversion recovery (B), T1-weighted (C), proton density-weighted (D), double inversion recovery (E), and phase-sensitive inversion recovery images in a patient with multiple sclerosis.

severity, independent of the number of MS plaques. Therefore, Glx could be an important biomarker of tissue damage in patients with MS, even in the absence of MS plaques. Increased *myo*-inositol levels, indicating increased glia, and decreased *N*-acetylaspartate and *N*-acetylaspartate-glutamate levels, indicating decreased neural tissue, were observed only in the normal-appearing WM of the MRI<sub>pos</sub> group. Quantitative MRI showed decreased R1 and increased PD in the normal-appearing WM of the MRI<sub>neg</sub> group when compared with WM in controls.<sup>2</sup> R1 and R2 values in the MRI<sub>pos</sub> group correlated significantly with disease severity. In addition to MS plaques, diffusely abnormal signal intensity with fuzzy borders on conventional T2-weighted images is often found in patients with MS. The signal intensity of this area is higher than that of normal-appearing WM but lower than that of focal MS plaques. This area is termed diffusely abnormal WM and is histologically related to axonal loss and decreased myelin.<sup>97</sup> Diffusely abnormal WM showed R1, R2, and PD values that were significantly different from those for normal-appearing WM; however, these values were similar in the MRI<sub>pos</sub> and MRI<sub>neg</sub> groups. These diffusely abnormal WM values lay in the intermediate range between those for normal-appearing WM and those for focal MS plaques. After transforming MRI scans of the brain in patients with MS into a standardized template, voxel-based analysis was performed to compare the findings with those obtained in healthy controls.<sup>87</sup> Decreased R1 and R2 and increased PD were observed in widespread areas, especially in the periventricular WM of patients with MS. Moreover, there was a strong correlation between changes in these values in the frontal WM and disease severity. In contrast, although the posterior corpus callosum was widely affected in patients with MS, it did not show a correlation with disease severity.

The myelin and edema model discussed earlier has been applied in patients with MS.<sup>3,75</sup> When compared with healthy controls, patients with MS had a decreased total myelin volume and an increased total

excess parenchymal water volume.<sup>75</sup> When template ROIs were applied, both GM and WM in patients with MS showed lower  $V_{MY}$  and higher  $V_{EPW}$  when compared with healthy controls.<sup>75</sup> In terms of focal MS plaques, this model may differentiate myelin loss and edema, unlike conventional T2-weighted or FLAIR images, which merely depict these processes as areas of hyperintensity. ROI analysis revealed that R1, R2, PD,  $V_{MY}$ , and  $V_{EPW}$  in normal-appearing WM, periplaque WM, and plaques were significantly different across these 3 areas, with periplaque WM showing intermediate values.<sup>3</sup> The percentage changes in these metrics in plaques and periplaque WM relative to normal-appearing WM were significantly more different from zero for  $V_{MY}$  and  $V_{EPW}$  than for R1, R2, and PD.<sup>75</sup> Therefore,  $V_{MY}$  and  $V_{EPW}$  are potentially more sensitive biomarkers of MS pathology than R1, R2, and PD.

### Brain Metastases

Contrast-enhanced MRI is useful for detecting brain metastases. T1-weighted images and newly developed T1IR images are the most widely used sequences for this purpose.<sup>98</sup> The ability of synthetic and conventional MRI to evaluate brain metastases was compared by Hagiwara et al.<sup>99</sup> The lesion-to-WM contrast and CNR were significantly higher for synthetic T1IR than for synthetic T1-weighted or conventional T1IR images. More lesions were detected by neuroradiologists on synthetic T1IR images than on synthetic T1-weighted or conventional T1IR images, although the difference was not statistically significant. Synthetic images, which are black-blood imaging, revealed some metastases that were hidden by flow-related artifacts in conventional T1IR images. Because synthetic images were not optimized for each patient in this research, a further study is needed to evaluate the detectability of brain metastases using synthetic MRI after adjusting the contrast for each patient. Because contrast-enhanced FLAIR can be

created after quantitative MRI, SyMRI is useful for detecting meningeal carcinomatosis even if it is not suspected before image acquisition (Fig. 6). Automatic detection of brain metastases may also be possible by applying the acquired quantitative data after administration of contrast to the R1-R2-PD grid in the normal brain.

### Sturge-Weber Syndrome

Sturge-Weber syndrome (SWS) is a rare neurocutaneous disorder that includes facial cutaneous vascular malformation and ipsilateral leptomeningeal angiomas that most often involves the parietal and occipital lobes.<sup>100</sup> Contrast-enhanced T1-weighted and fluid-attenuated inversion recovery (FLAIR) images show leptomeningeal enhancement on the affected side. Contrast-enhanced synthetic DIR images, which suppress signals of bone marrow fat and CSF, have demonstrated both dural and leptomeningeal enhancement.<sup>46</sup> Dural angiomas in a patient with SWS has been shown pathologically,<sup>101</sup> but dural enhancement has rarely been reported radiologically. Synthetic MRI is useful for showing dural lesions on DIR images that are not routinely acquired.

Before myelination is complete in the developing brain, the WM on the affected side in SWS shows relative hypointensity on T2-weighted imaging when compared with the contralateral side. There are several explanations for this phenomenon, and “accelerated myelination” is one of the possibilities.<sup>102</sup> SyMRI was applied to a 4-month-old patient with SWS, and the WM on the affected side was more hypointense on synthetic T2-weighted imaging than on the contralateral side.<sup>47</sup> The R1 and R2 of WM were higher and the PD of the WM was lower on the affected side than on the contralateral side. DIR imaging that suppresses unmyelinated WM and CSF showed this “accelerated myelination” area as hyperintensity. Detection of these WM changes may be useful for early diagnosis of SWS and improve the prognosis by early initiation of treatment.

### Idiopathic Normal Pressure Hydrocephalus

Idiopathic normal pressure hydrocephalus (iNPH) is a disease characterized by gait disturbance, cognitive impairment, and urinary incontinence.<sup>103</sup> Enlarged ventricles are observed on MRI and are usually measured by the Evans Index,<sup>104</sup> which is the ratio of the maximum transverse diameter of the frontal horns of the lateral ventricles to that of the internal skull. However, after shunting, more than half of patients who show clinical improvement are found to have little or no change in this index.<sup>105</sup> Therefore, a more sensitive measure of ventricular size

is required. Manual segmentation is the criterion standard but is time-consuming and unrealistic for use in daily practice. In a study by Virhammar et al,<sup>106</sup> iNPH was evaluated by quantitative MRI performed before and after lumbar puncture with drainage. After lumbar puncture, there were significant decreases in the volume of the lateral ventricles measured by manual segmentation and CSF volume measured by SyMRI and a significant increase in BPF measured by SyMRI. Cerebrospinal fluid volume and BPF correlated significantly with the volume of the lateral ventricles. Therefore, BPF and CSF volume measured by SyMRI may be useful for objective monitoring of the course of iNPH.

### Meningitis

Contrast-enhanced MRI is the imaging method of choice for evaluation of meningitis.<sup>107</sup> Although contrast-enhanced FLAIR is more sensitive to meningitis than contrast-enhanced T1-weighted imaging, it is not routinely performed in many institutions.<sup>108</sup> Given that synthetic MRI enables creation of FLAIR images after image acquisition, synthetic MRI may increase the sensitivity of meningitis.<sup>109</sup>

### Postmortem Imaging

Computed tomography (CT) has been used in many institutions for postmortem imaging.<sup>110</sup> The obvious advantage of CT is its short acquisition time for 3-dimensional volume data that can be reformatted in any plane and volume rendered. The major disadvantage of CT for postmortem purposes is its poor ability to discriminate soft tissues and internal organs, except for the lungs.<sup>111</sup> Although the scanning time is much longer than that needed for CT, whole-body quantitative MRI (90 minutes) can also be performed by isovoxel acquisition that enables reformatting and volume rendering.<sup>112</sup> The problem with postmortem MRI is that the temperature of a cadaver varies substantially depending on the time lapse between death and image acquisition, and the relaxation behavior, especially the T1 value, changes accordingly.<sup>112</sup> In quantitative MRI, correction formulae for relaxation values have been investigated for cadaver temperatures and established in many body tissues and organs.<sup>113–116</sup> After correction for temperature, quantitative MRI data can be used to create optimum contrast-weighted images in optimal image planes with better soft tissue discrimination than in CT. The quantitative values can be projected onto a R1-R2-PD space, which may enable measurement of absolute deviation of a specific voxel from normal tissue and automatic detection of pathology (eg, hematoma or

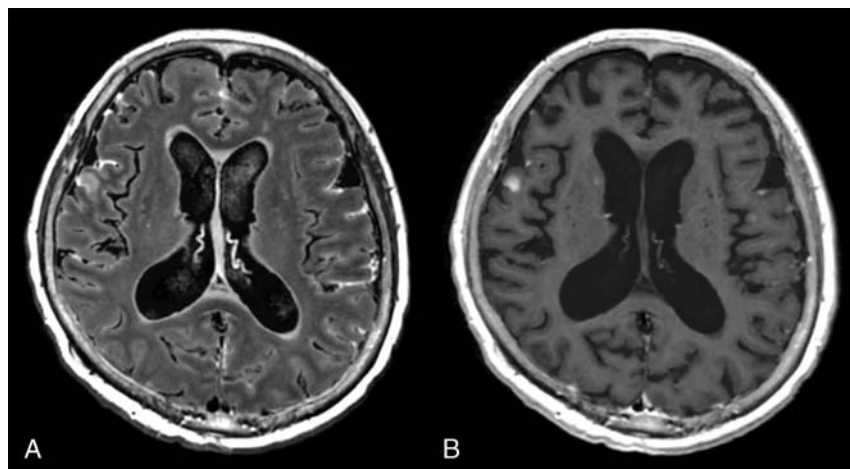


**FIGURE 6.** Images of a patient with multiple brain metastases and meningeal carcinomatosis. Contrast-enhanced synthetic fluid-attenuated inversion recovery (FLAIR) (A) shows meningeal carcinomatosis more clearly than a synthetic T1-weighted image (B). Contrast-enhanced FLAIR images are not acquired routinely in many institutions, and creating a FLAIR image after quantitative MRI is an advantage of synthetic MRI.

infarction) by artificial intelligence. It is also possible to discern various anatomic structures based on the quantitative data. Correction of cadaver temperature to 37°C has been shown to enable better differentiation between types of body fluid (eg, blood and CSF).<sup>114</sup> For whole-body acquisition, the table has to be moved step by step through the scanner and the images acquired have to be merged. Because of its dependence on PD, postmortem MRI may not be useful for severely mummified corpses<sup>117</sup> or for corpses on which adipocere has formed<sup>118</sup> but is still valid for putrefied corpses.<sup>112</sup>

## CONCLUSIONS

Rapid simultaneous acquisition of R1, R2, and PD can now be performed in about 6 minutes, based on QRAPMASTER pulse sequence. The quantitative values can be used for automatic segmentation, volumetry, and estimation of myelin volume. Any contrast-weighted image can be created based on these values by virtually setting the repetition time, echo time, and inversion recovery time. The quality of the synthetic images is comparable with that of conventional images except for the synthetic FLAIR image, which is sometimes degraded by artifacts. SyMRI has been evaluated for MS, brain metastases, SWS, iNPH, meningitis, and postmortem imaging, with promising results.

## ACKNOWLEDGMENTS

The authors thank Mr Nao Takano, Mr Nozomi Hamasaki, and Mr Shuji Sato for helping us gather the data.

## REFERENCES

- Wartjes JB, Leinhard OD, West J, et al. Rapid magnetic resonance quantification on the brain: optimization for clinical usage. *Magn Reson Med*. 2008;60:320–329.
- West J, Aalto A, Tisell A, et al. Normal appearing and diffusely abnormal white matter in patients with multiple sclerosis assessed with quantitative MR. *PLoS One*. 2014;9:e95161.
- Hagiwara A, Hori M, Yokoyama K, et al. Utility of a multiparametric quantitative MRI model that assesses myelin and edema for evaluating plaques, periplaque white matter, and normal-appearing white matter in patients with multiple sclerosis: a feasibility study. *AJNR Am J Neuroradiol*. 2017;38:237–242.
- Wagner MC, Lukas P, Herzog M, et al. MRI and proton-NMR relaxation times in diagnosis and therapeutic monitoring of squamous cell carcinoma. *Eur Radiol*. 1994;4:314–323.
- Drain LE. A direct method of measuring nuclear spin-lattice relaxation times. *Proc Phys Soc A*. 1949;62:301–306.
- Hahn EL. An accurate nuclear magnetic resonance method for measuring spin-lattice relaxation times. *Phys Rev*. 1949;76:145–146.
- Hahn EL. Spin echoes. *Phys Rev*. 1950;80:580–594.
- Deichmann R. Fast high-resolution T1 mapping of the human brain. *Magn Reson Med*. 2005;54:20–27.
- Henderson E, McKinnon G, Lee TY, et al. A fast 3D look-locker method for volumetric T1 mapping. *Magn Reson Imaging*. 1999;17:1163–1171.
- Ordidge RJ, Gibbs P, Chapman B, et al. High-speed multislice T1 mapping using inversion-recovery echo-planar imaging. *Magn Reson Med*. 1990;16:238–245.
- Zhu DC, Penn RD. Full-brain T1 mapping through inversion recovery fast spin echo imaging with time-efficient slice ordering. *Magn Reson Med*. 2005;54:725–731.
- Clare S, Jezzard P. Rapid T(1) mapping using multislice echo planar imaging. *Magn Reson Med*. 2001;45:630–634.
- Neeb H, Zilles K, Shah NJ. A new method for fast quantitative mapping of absolute water content in vivo. *Neuroimage*. 2006;31:1156–1168.
- Deoni SC, Peters TM, Rutt BK. High-resolution T1 and T2 mapping of the brain in a clinically acceptable time with DESPOT1 and DESPOT2. *Magn Reson Med*. 2005;53:237–241.
- Whittall KP, MacKay AL, Graeb DA, et al. In vivo measurement of T2 distributions and water contents in normal human brain. *Magn Reson Med*. 1997;37:34–43.
- McKenzie CA, Chen Z, Drost DJ, et al. Fast acquisition of quantitative T2 maps. *Magn Reson Med*. 1999;41:208–212.
- Maier CF, Tan SG, Hariharan H, et al. T2 quantitation of articular cartilage at 1.5 T. *J Magn Reson Imaging*. 2003;17:358–364.
- Dahnke H, Schaeffter T. Limits of detection of SPIO at 3.0 T using T2 relaxometry. *Magn Reson Med*. 2005;53:1202–1206.
- Westwood M, Anderson LJ, Firmin DN, et al. A single breath-hold multiecho T2\* cardiovascular magnetic resonance technique for diagnosis of myocardial iron overload. *J Magn Reson Imaging*. 2003;18:33–39.
- Pepe A, Positano V, Santarelli MF, et al. Multislice multiecho T2\* cardiovascular magnetic resonance for detection of the heterogeneous distribution of myocardial iron overload. *J Magn Reson Imaging*. 2006;23:662–668.
- Kumar R, Delshad S, Woo MA, et al. Age-related regional brain T2-relaxation changes in healthy adults. *J Magn Reson Imaging*. 2012;35:300–308.
- Ehnes P, Seiberlich N, Ma D, et al. IR TrueFISP with a golden-ratio-based radial readout: fast quantification of T1, T2, and proton density. *Magn Reson Med*. 2013;69:71–81.
- Ma D, Gulani V, Seiberlich N, et al. Magnetic resonance fingerprinting. *Nature*. 2013;495:187–192.
- Krauss W, Gunnarsson M, Andersson T, et al. Accuracy and reproducibility of a quantitative magnetic resonance imaging method for concurrent measurements of tissue relaxation times and proton density. *Magn Reson Imaging*. 2015;33:584–591.
- Bobman SA, Riederer SJ, Lee JN, et al. Cerebral magnetic resonance image synthesis. *AJNR Am J Neuroradiol*. 1985;6:265–269.
- Riederer SJ, Lee JN, Farzana F, et al. Magnetic resonance image synthesis. Clinical implementation. *Acta Radiol Suppl*. 1986;369:466–468.
- Hagiwara A, Hori M, Yokoyama K, et al. Synthetic MRI in the detection of multiple sclerosis plaques. *AJNR Am J Neuroradiol*. 2017;38:257–263.
- West H, Leach JL, Jones BV, et al. Clinical validation of synthetic brain MRI in children: initial experience. *Neuroradiology*. 2016;59:43–50.
- Ambarki K, Lindqvist T, Wahlin A, et al. Evaluation of automatic measurement of the intracranial volume based on quantitative MR imaging. *AJNR Am J Neuroradiol*. 2012;33:1951–1956.
- Granberg T, Uppman M, Hashim F, et al. Clinical feasibility of synthetic MRI in multiple sclerosis: a diagnostic and volumetric validation study. *AJNR Am J Neuroradiol*. 2016;37:1023–1029.
- Vågberg M, Lindqvist T, Ambarki K, et al. Automated determination of brain parenchymal fraction in multiple sclerosis. *AJNR Am J Neuroradiol*. 2013;34:498–504.
- Labadie C, Lee JH, Rooney WD, et al. Myelin water mapping by spatially regularized longitudinal relaxographic imaging at high magnetic fields. *Magn Reson Med*. 2014;71:375–387.
- Wartjes JB, Engström M, Tisell A, et al. Brain characterization using normalized quantitative magnetic resonance imaging. *PLoS One*. 2013;8:e70864.
- Hasan KM, Walimuni IS, Abid H, et al. Human brain atlas-based multimodal MRI analysis of volumetry, diffusometry, relaxometry and lesion distribution in multiple sclerosis patients and healthy adult controls: implications for understanding the pathogenesis of multiple sclerosis and consolidation of quantitative MRI results in MS. *J Neurol Sci*. 2012;313:99–109.
- Bernasconi A, Bernasconi N, Caramanos Z, et al. T2 relaxometry can lateralize mesial temporal lobe epilepsy in patients with normal MRI. *Neuroimage*. 2000;12:739–746.
- Hasan KM, Walimuni IS, Abid H, et al. Multi-modal quantitative MRI investigation of brain tissue neurodegeneration in multiple sclerosis. *J Magn Reson Imaging*. 2012;35:1300–1311.
- Neema M, Stankiewicz J, Arora A, et al. T1- and T2-based MRI measures of diffuse gray matter and white matter damage in patients with multiple sclerosis. *J Neuroimaging*. 2007;17(suppl 1):16S–21S.
- Larsson HB, Frederiksen J, Petersen J, et al. Assessment of demyelination, edema, and gliosis by in vivo determination of T1 and T2 in the brain of patients with acute attack of multiple sclerosis. *Magn Reson Med*. 1989;11:337–348.
- Larsson HB, Frederiksen J, Kjaer L, et al. In vivo determination of T1 and T2 in the brain of patients with severe but stable multiple sclerosis. *Magn Reson Med*. 1988;7:43–55.
- Ymazal J, Righini A, Brooks RA, et al. T1 and T2 in the brain of healthy subjects, patients with Parkinson disease, and patients with multiple system atrophy: relation to iron content. *Radiology*. 1999;211:489–495.
- Friedman SD, Shaw DW, Artru AA, et al. Regional brain chemical alterations in young children with autism spectrum disorder. *Neurology*. 2003;60:100–107.
- Williamson P, Pelz D, Merskey H, et al. Frontal, temporal, and striatal proton relaxation times in schizophrenic patients and normal comparison subjects. *Am J Psychiatry*. 1992;149:549–551.
- Mamere AE, Saraiva LA, Matos AL, et al. Evaluation of delayed neuronal and axonal damage secondary to moderate and severe traumatic brain injury using quantitative MR imaging techniques. *AJNR Am J Neuroradiol*. 2009;30:947–952.

44. Waldman AD. Magnetic resonance imaging of brain tumors—time to quantify. *Discov Med*. 2010;9:7–12.
45. Oh J, Cha S, Aiken AH, et al. Quantitative apparent diffusion coefficients and T2 relaxation times in characterizing contrast enhancing brain tumors and regions of peritumoral edema. *J Magn Reson Imaging*. 2005;21:701–708.
46. Hagiwara A, Nakazawa M, Andica C, et al. Dural enhancement in a patient with Sturge-Weber syndrome revealed by double inversion recovery contrast using synthetic MRI. *Magn Reson Med Sci*. 2016;15:151–152.
47. Andica C, Hagiwara A, Nakazawa M, et al. The advantage of synthetic MRI for the visualization of early white matter change in an infant with Sturge-Weber syndrome. *Magn Reson Med Sci*. 2016;15:347–348.
48. Betts AM, Leach JL, Jones BV, et al. Brain imaging with synthetic MR in children: clinical quality assessment. *Neuroradiology*. 2016;58:1017–1026.
49. Maitra R, Riddles JJ. Synthetic magnetic resonance imaging revisited. *IEEE Trans Med Imaging*. 2010;29:895–902.
50. Blystad I, Wamtsjes JB, Smedby O, et al. Synthetic MRI of the brain in a clinical setting. *Acta Radiol*. 2012;53:1158–1163.
51. Simmons A, Westman E, Muehlboeck S, et al. MRI measures of Alzheimer's disease and the AddNeuroMed study. *Ann N Y Acad Sci*. 2009;1180:47–55.
52. Kim GH, Lee JH, Seo SW, et al. Hippocampal volume and shape in pure subcortical vascular dementia. *Neurobiol Aging*. 2015;36:485–491.
53. Rovira A, Leon A. MR in the diagnosis and monitoring of multiple sclerosis: an overview. *Eur J Radiol*. 2008;67:409–414.
54. Mikheev A, Nevsky G, Govindan S, et al. Fully automatic segmentation of the brain from T1-weighted MRI using Bridge Burner algorithm. *J Magn Reson Imaging*. 2008;27:1235–1241.
55. Andersen AH, Zhang Z, Avison MJ, et al. Automated segmentation of multispectral brain MR images. *J Neurosci Methods*. 2002;122:13–23.
56. Choi HS, Haynor DR, Kim Y. Partial volume tissue classification of multichannel magnetic resonance images—a mixel model. *IEEE Trans Med Imaging*. 1991;10:395–407.
57. Shattuck DW, Sandor-Leahy SR, Schaper KA, et al. Magnetic resonance image tissue classification using a partial volume model. *Neuroimage*. 2001;13:856–876.
58. West J, Wamtsjes JB, Lundberg P. Novel whole brain segmentation and volume estimation using quantitative MRI. *Eur Radiol*. 2012;22:998–1007.
59. Alfano B, Brunetti A, Covelli EM, et al. Unsupervised, automated segmentation of the normal brain using a multispectral relaxometric magnetic resonance approach. *Magn Reson Med*. 1997;37:84–93.
60. Breger RK, Wehrli FW, Charles HC, et al. Reproducibility of relaxation and spindensity parameters in phantoms and the human brain measured by MR imaging at 1.5 T. *Magn Reson Med*. 1986;3:649–662.
61. Bottomley PA, Hardy CJ, Argersinger RE, et al. A review of 1H nuclear magnetic resonance relaxation in pathology: are T1 and T2 diagnostic? *Med Phys*. 1987;14:1–37.
62. Fletcher LM, Barsotti JB, Hornak JP. A multispectral analysis of brain tissues. *Magn Reson Med*. 1993;29:623–630.
63. Wamtsjes JB, Tisell A, Landtblom AM, et al. Effects of gadolinium contrast agent administration on automatic brain tissue classification of patients with multiple sclerosis. *AJNR Am J Neuroradiol*. 2014;35:1330–1336.
64. Vågberg M, Ambarki K, Lindqvist T, et al. Brain parenchymal fraction in an age-stratified healthy population - determined by MRI using manual segmentation and three automated segmentation methods. *J Neuroradiol*. 2016;43:384–391.
65. Pfefferbaum A, Rohlfing T, Rosenbloom MJ, et al. Combining atlas-based parcellation of regional brain data acquired across scanners at 1.5 T and 3.0 T field strengths. *Neuroimage*. 2012;60:940–951.
66. West J, Blystad I, Engstrom M, et al. Application of quantitative MRI for brain tissue segmentation at 1.5 T and 3.0 T field strengths. *PLoS One*. 2013;8:e74795.
67. Hocq A, Brouette N, Saussez S, et al. Variable-field relaxometry of iron-containing human tissues: a preliminary study. *Contrast Media Mol Imaging*. 2009;4:157–164.
68. Louveau A, Smirnov I, Keyes TJ, et al. Structural and functional features of central nervous system lymphatic vessels. *Nature*. 2015;523:337–341.
69. Provencher SW. Estimation of metabolite concentrations from localized in vivo proton NMR spectra. *Magn Reson Med*. 1993;30:672–679.
70. Tisell A, Leinhard OD, Wamtsjes JB, et al. Procedure for quantitative (1H) magnetic resonance spectroscopy and tissue characterization of human brain tissue based on the use of quantitative magnetic resonance imaging. *Magn Reson Med*. 2013;70:905–915.
71. Caramanos Z, Narayanan S, Arnold DL. 1H-MRS quantification of tNA and tCr in patients with multiple sclerosis: a meta-analytic review. *Brain*. 2005;128:2483–2506.
72. Hennig J, Pfister H, Ernst T, et al. Direct absolute quantification of metabolites in the human brain with in vivo localized proton spectroscopy. *NMR Biomed*. 1992;5:193–199.
73. Keevil SF, Barbiroli B, Brooks JC, et al. Absolute metabolite quantification by in vivo NMR spectroscopy: II. A multicentre trial of protocols for in vivo localised proton studies of human brain. *Magn Reson Imaging*. 1998;16:1093–1106.
74. Tisell A, Leinhard OD, Wamtsjes JB, et al. Increased concentrations of glutamate and glutamine in normal-appearing white matter of patients with multiple sclerosis and normal MR imaging brain scans. *PLoS One*. 2013;8:e61817.
75. Wamtsjes M, Engström M, Tisell A, et al. Modeling the presence of myelin and edema in the brain based on multi-parametric quantitative MRI. *Front Neurol*. 2016;7:16.
76. Bjarnason TA, Vavasour IM, Chia CL, et al. Characterization of the NMR behavior of white matter in bovine brain. *Magn Reson Med*. 2005;54:1072–1081.
77. Laule C, Leung E, Lis DK, et al. Myelin water imaging in multiple sclerosis: quantitative correlations with histopathology. *Mult Scler*. 2006;12:747–753.
78. Zhang H, Schneider T, Wheeler-Kingshott CA, et al. NODDI: practical in vivo neurite orientation dispersion and density imaging of the human brain. *Neuroimage*. 2012;61:1000–1016.
79. Stikov N, Campbell JS, Stroh T, et al. In vivo histology of the myelin g-ratio with magnetic resonance imaging. *Neuroimage*. 2015;118:397–405.
80. West KL, Kelm ND, Carson RP, et al. Myelin volume fraction imaging with MRI. *Neuroimage*. 2016. [Epub ahead of print].
81. Alonso-Ortiz E, Levesque IR, Pike GB. MRI-based myelin water imaging: a technical review. *Magn Reson Med*. 2015;73:70–81.
82. Glasser MF, Van Essen DC. Mapping human cortical areas in vivo based on myelin content as revealed by T1- and T2-weighted MRI. *J Neurosci*. 2011;31:11597–11616.
83. Bonzano L, Roccatagliata L, Mancardi GL, et al. Gadolinium-enhancing or active T2 magnetic resonance imaging lesions in multiple sclerosis clinical trials? *Mult Scler*. 2009;15:1043–1047.
84. Nelson F, Poonawalla AH, Hou P, et al. Improved identification of intracortical lesions in multiple sclerosis with phase-sensitive inversion recovery in combination with fast double inversion recovery MR imaging. *AJNR Am J Neuroradiol*. 2007;28:1645–1649.
85. Bedell BJ, Narayana PA. Implementation and evaluation of a new pulse sequence for rapid acquisition of double inversion recovery images for simultaneous suppression of white matter and CSF. *J Magn Reson Imaging*. 1998;8:544–547.
86. Hou P, Hasan KM, Sitton CW, et al. Phase-sensitive T1 inversion recovery imaging: a time-efficient interleaved technique for improved tissue contrast in neuroimaging. *AJNR Am J Neuroradiol*. 2005;26:1432–1438.
87. Engström M, Wamtsjes JB, Tisell A, et al. Multi-parametric representation of voxel-based quantitative magnetic resonance imaging. *PLoS One*. 2014;9:e111688.
88. Rudick RA, Fisher E, Lee JC, et al. Use of the brain parenchymal fraction to measure whole brain atrophy in relapsing-remitting MS. Multiple Sclerosis Collaborative Research Group. *Neurology*. 1999;53:1698–1704.
89. Kassubek J, Tumani H, Ecker D, et al. Age-related brain parenchymal fraction is significantly decreased in young multiple sclerosis patients: a quantitative MRI study. *Neuroreport*. 2003;14:427–430.
90. Fisher E, Rudick RA, Simon JH, et al. Eight-year follow-up study of brain atrophy in patients with MS. *Neurology*. 2002;59:1412–1420.
91. De Stefano N, Airas L, Grigoriadis N, et al. Clinical relevance of brain volume measures in multiple sclerosis. *CNS Drugs*. 2014;28:147–156.
92. Vrenken H, Geurts JJ, Knol DL, et al. Whole-brain T1 mapping in multiple sclerosis: global changes of normal-appearing gray and white matter. *Radiology*. 2006;240:811–820.
93. Prince MR, Zhang H, Zou Z, et al. Incidence of immediate gadolinium contrast media reactions. *AJR Am J Roentgenol*. 2011;196:W138–W143.
94. Kanda T, Fukusato T, Matsuda M, et al. Gadolinium-based contrast agent accumulates in the brain even in subjects without severe renal dysfunction: evaluation of autopsy brain specimens with inductively coupled plasma mass spectroscopy. *Radiology*. 2015;276:228–232.
95. Blystad I, Håkansson I, Tisell A, et al. Quantitative MRI for analysis of active multiple sclerosis lesions without gadolinium-based contrast agent. *AJNR Am J Neuroradiol*. 2016;37:94–100.
96. Barkhof F. The clinico-radiological paradox in multiple sclerosis revisited. *Curr Opin Neurol*. 2002;15:239–245.
97. Seewann A, Vrenken H, van der Valk P, et al. Diffusely abnormal white matter in chronic multiple sclerosis: imaging and histopathologic analysis. *Arch Neurol*. 2009;66:601–609.
98. Qian YF, Yu CL, Zhang C, et al. MR T1-weighted inversion recovery imaging in detecting brain metastases: could it replace T1-weighted spin-echo imaging? *AJNR Am J Neuroradiol*. 2008;29:701–704.

99. Hagiwara A, Hori M, Suzuki M, et al. Contrast-enhanced synthetic MRI for the detection of brain metastases. *Acta Radiol Open*. 2016;5:2058460115626757.
100. Thomas-Sohl KA, Vaslow DF, Maria BL. Sturge-Weber syndrome: a review. *Pediatr Neurol*. 2004;30:303–310.
101. Di Rocco C, Tamburrini G. Sturge-Weber syndrome. *Childs Nerv Syst*. 2006;22:909–921.
102. Adamsbaum C, Pinton F, Rolland Y, et al. Accelerated myelination in early Sturge-Weber syndrome: MRI-SPECT correlations. *Pediatr Radiol*. 1996;26:759–762.
103. Adams RD, Fisher CM, Hakim S, et al. Symptomatic occult hydrocephalus with “normal” cerebrospinal-fluid pressure. A treatable syndrome. *N Engl J Med*. 1965;273:117–126.
104. Evans WA. An encephalographic ratio for estimating ventricular enlargement and cerebral atrophy. *Arch Neur Psych*. 1942;47:931–937.
105. Meier U, Paris S, Grawe A, et al. Is there a correlation between operative results and change in ventricular volume after shunt placement? A study of 60 cases of idiopathic normal-pressure hydrocephalus. *Neuroradiology*. 2003;45:377–380.
106. Virhammar J, Warntjes M, Laurell K, et al. Quantitative MRI for rapid and user-independent monitoring of intracranial CSF volume in hydrocephalus. *AJNR Am J Neuroradiol*. 2016;37:797–801.
107. Hazany S, Go JL, Law M. Magnetic resonance imaging of infectious meningitis and ventriculitis in adults. *Top Magn Reson Imaging*. 2014;23:315–325.
108. Splendiani A, Puglielli E, De Amicis R, et al. Contrast-enhanced FLAIR in the early diagnosis of infectious meningitis. *Neuroradiology*. 2005;47:591–598.
109. Andica C, Hagiwara A, Nakazawa M, et al. Synthetic MR imaging in the diagnosis of bacterial meningitis. *Magn Reson Med Sci*. 2016. [Epub ahead of print].
110. Poulsen K, Simonsen J. Computed tomography as routine in connection with medico-legal autopsies. *Forensic Sci Int*. 2007;171:190–197.
111. Shiotani S, Kohno M, Ohashi N, et al. Non-traumatic postmortem computed tomographic (PMCT) findings of the lung. *Forensic Sci Int*. 2004;139:39–48.
112. Jackowski C, Warntjes MJ, Kihlberg J, et al. Quantitative MRI in isotropic spatial resolution for forensic soft tissue documentation. Why and how? *J Forensic Sci*. 2011;56:208–215.
113. Zech WD, Hottinger AL, Schwendener N, et al. Post-mortem 1.5 T MR quantification of regular anatomical brain structures. *Int J Legal Med*. 2016;130:1071–1080.
114. Zech WD, Schwendener N, Persson A, et al. Postmortem quantitative 1.5-T MRI for the differentiation and characterization of serous fluids, blood, CSF, and putrefied CSF. *Int J Legal Med*. 2015;129:1127–1136.
115. Zech WD, Schwendener N, Persson A, et al. Temperature dependence of post-mortem MR quantification for soft tissue discrimination. *Eur Radiol*. 2015;25:2381–2389.
116. Schwendener N, Jackowski C, Persson A, et al. Detection and differentiation of early acute and following age stages of myocardial infarction with quantitative post-mortem cardiac 1.5 T MR. *Forensic Sci Int*. 2017;270:248–254.
117. Jackowski C, Bolliger S, Thali MJ. Common and unexpected findings in mummies from ancient Egypt and South America as revealed by CT. *Radiographics*. 2008;28:1477–1492.
118. Jackowski C, Thali M, Sonnenschein M, et al. Adipocere in postmortem imaging using multislice computed tomography (MSCT) and magnetic resonance imaging (MRI). *Am J Forensic Med Pathol*. 2005;26:360–364.